

Energy-consistent finite difference schemes for compressible hydrodynamics and magnetohydrodynamics using nonlinear filtering

Haruhisa Iijima

*Institute for Space-Earth Environmental Research, Nagoya University, Furocho, Chikusa-ku, Nagoya, Aichi
464-8601, Japan*

National Astronomical Observatory of Japan, 2-21-1 Osawa, Mitaka, Tokyo 181-8588, Japan

Abstract

In this paper, an energy-consistent finite difference scheme for the compressible hydrodynamic and magnetohydrodynamic (MHD) equations is introduced. For the compressible magnetohydrodynamics, an energy-consistent finite difference formulation is derived using the product rule for the spatial difference. The conservation properties of the internal, kinetic, and magnetic energy equations can be satisfied in the discrete level without explicitly solving the total energy equation. The shock waves and discontinuities in the numerical solution are stabilized by nonlinear filtering schemes. An energy-consistent discretization of the filtering schemes is also derived by introducing the viscous and resistive heating rates. The resulting energy-consistent formulation can be implemented with the various kinds of central difference, nonlinear filtering, and time integration schemes. The second- and fifth-order schemes are implemented based on the proposed formulation. The conservation properties and the robustness of the present schemes are demonstrated via one- and two-dimensional numerical tests. The proposed schemes successfully handle the most stringent problems in extremely high Mach number and low beta conditions.

Keywords: Hydrodynamics, Magnetohydrodynamics, Computational plasma physics, Finite differences, Shock capturing, Spatial filtering, Skew-symmetric form, Secondary conservative

1. Introduction

The fully conservative finite difference scheme has been used as a tool for the numerical simulation of the incompressible flow due to its very small numerical dissipations and the stability in the long-term simulations [1, 2, 3]. In such schemes, the quadratic split form (also known as the skew-symmetric split form) of the convective term is used to achieve the kinetic

Email address: h.iijima@isee.nagoya-u.ac.jp (Haruhisa Iijima)

energy conservation in the discrete sense while maintaining the momentum conservation without directly solving the kinetic energy equation. The quadratic and cubic split operators can also reduce the aliasing error produced in the product of the multiple variables [4, 5].

Several researchers have attempted to extend the split form of the convective term to the low Mach number flows (see a review by Pirozzoli [6]). The Jameson-Schmidt-Turkel scheme [7] implicitly used the quadratic split operator in the finite volume formulation [8]. The kinetic energy preserving (KEP) scheme is constructed using the quadratic split operator [9, 10, 11]. The quadratic split operator can even achieve the consistency between the internal energy and kinetic energy in the discrete sense [12, 13]. The concept of the quadratic split operator can be extended into the nonuniform cylindrical coordinates [14]. The temporal derivatives can be also discretized using the quadratic split operator to obtain the spatiotemporal conservation properties [13]. The conservation of the entropy can also be achieved in addition to the energy-consistency [15].

Fewer studies investigated the application of the energy-consistent schemes to the high Mach number flows. In high-speed flow simulations, additional numerical diffusion schemes are required to stabilize the shock waves and discontinuities. Jameson et al. [7] used an artificial viscosity to stabilize their skew-symmetric finite volume scheme. Ducros et al. [8] suggested the hybridization between the central and upwind schemes. Yee [16] employed a nonlinear filtering approach for the entropy conserving scheme. However, the energy consistency of these diffusion schemes was rarely discussed explicitly, except in the work by Shiroto et al. [17].

In recent years, the application of the quadratic split operator has increasingly been applied to the plasma physics, to achieve the secondary conservation properties. Ni et al. [18, 19, 20] constructed the current density conservative scheme for the incompressible magnetohydrodynamic (MHD) simulations. Shiroto et al. [17] applied the approach to the two-temperature plasma flows. There are several applications of the quadratic split operator on the kinetic plasma equations [21, 22]. However, an energy-consistent scheme for application to compressible MHD simulations has not yet been constructed.

In the compressible MHD simulations, the consistency between the internal, kinetic, and magnetic energies is essential to accurately reproduce the plasma dynamics and energetics. Many numerical schemes solve the total (internal + kinetic + magnetic) energy equation to satisfy the jump condition near the shocks and discontinuities. However, in such schemes, the discretization errors of the kinetic and magnetic energy equations are imposed on the internal energy. As a result, the evolution of the internal energy becomes inevitably erroneous when the internal energy is much smaller than the kinetic or magnetic energy. Such numerical simulations yield energetically inaccurate solutions, such as the negative pressure.

This study aims to construct an energy-consistent formulation for the compressible hydrodynamic and MHD equations while taking account the nonlinear filtering. Hence, an fully energy-consistent finite difference scheme is devised. Our implementation of this scheme with the appropriate nonlinear filtering scheme provides superior numerical robustness, especially in the extremely high Mach number and low plasma beta (internal over magnetic energies) conditions.

This paper is organized as follows. Section 2 presents the energy-consistent formulations

of the governing equations as well as the nonlinear filtering flux. Note that the proposed formulation is independent from the details of the finite difference operators, the filtering flux, and the temporal integration method. Section 3 describes our implementation of the proposed scheme. In Section 4, several numerical tests are performed, especially focusing on the energy-consistency and numerical robustness of the proposed scheme. Finally, Section 5 presents the conclusions of this article.

2. Energy-consistent scheme for compressible hydrodynamic and MHD equations

2.1. Basic equations and analytical requirements

The basic equations of the ideal, fully compressible MHD system in the Cartesian coordinates x_i ($i = 1, 2, 3$) can be written in a conservative form as

$$\frac{\partial \rho}{\partial t} + \frac{\partial \rho V_j}{\partial x_j} = 0, \quad (1)$$

$$\frac{\partial \rho V_i}{\partial t} + \frac{\partial \rho V_j V_i}{\partial x_j} + \frac{\partial P}{\partial x_i} + \frac{1}{2} \frac{\partial B_j B_j}{\partial x_i} - \frac{\partial B_i B_j}{\partial x_j} = 0, \quad (2)$$

$$\frac{\partial}{\partial t} \left(e + \frac{1}{2} \rho V_i V_i + \frac{1}{2} B_i B_i \right) + \frac{\partial}{\partial x_j} \left[\left(e + P + \frac{1}{2} \rho V_i V_i + B_i B_i \right) V_j - B_j B_i V_i \right] = 0, \quad (3)$$

$$\frac{\partial B_i}{\partial t} + \frac{\partial (V_j B_i - V_i B_j)}{\partial x_j} = 0. \quad (4)$$

Here, the summation rule is assumed. The variables ρ , e , and P represent the mass density, the internal energy density, and the gas pressure, respectively, and V_i and B_i represent the x_i -component of the velocity field and the magnetic field, respectively. The absence of the magnetic monopole provides a constraint on the magnetic field:

$$\frac{\partial B_j}{\partial x_j} = 0. \quad (5)$$

The above equations are closed by the equation of states for the gas pressure $P(\rho, e)$. The hydrodynamic equations can be derived by neglecting all components of the magnetic field (setting $B_i = 0$ for any i).

The conservation law of the momentum expressed in Eqs. (2) can be rewritten as

$$\frac{\partial \rho V_i}{\partial t} + \frac{\partial \rho V_j V_i}{\partial x_j} = F_i^P + F_i^L, \quad (6)$$

where F_i^P is the pressure gradient force in the i -th direction

$$F_i^P = - \frac{\partial P}{\partial x_i} \quad (7)$$

and F_i^L is the Lorentz force in the i -th direction

$$F_i^{L,c} = -B_j \left(\frac{\partial B_j}{\partial x_i} - \frac{\partial B_i}{\partial x_j} \right) + B_i \frac{\partial B_j}{\partial x_j}, \quad (8)$$

respectively. The last term of Eq. (8) disappears when the solenoidal condition of Eq. (5) is satisfied. The resultant Lorentz force can be written as

$$F_i^L = -B_j \left(\frac{\partial B_j}{\partial x_i} - \frac{\partial B_i}{\partial x_j} \right). \quad (9)$$

In this form, the Lorentz force is normal to the direction of the magnetic field ($F_i^L B_i = 0$).

In numerical simulations, the solenoidal constraint of the magnetic field is sometimes violated due to discretization error. Violation of the $\nabla \cdot \mathbf{B} = 0$ condition produces the inconsistency between the conservative and non-conservative Lorentz force, which yields artificial field-aligned forces $B_i \nabla \cdot \mathbf{B}$.

From the basic equations (Eqs. (1)-(4)), three independent energy equations, namely, internal, kinetic, and magnetic energy equations, can be derived:

$$\frac{\partial e}{\partial t} + \frac{\partial (e + P) V_j}{\partial x_j} = -W^P, \quad (10)$$

$$\frac{\partial (\rho V_i V_i / 2)}{\partial t} + \frac{\partial (\rho V_i V_i V_j / 2)}{\partial x_j} = W^P + W^L, \quad (11)$$

$$\frac{\partial (B_i B_i / 2)}{\partial t} + \frac{\partial (B_i B_i V_j - B_j B_i V_i)}{\partial x_j} = -W^L, \quad (12)$$

respectively. Here, we defined the work done by the pressure gradient force

$$W^P = V_i F_i^P \quad (13)$$

and the work done by the Lorentz force

$$W^L = V_i F_i^L. \quad (14)$$

It is clear that the equations for the internal, kinetic, and magnetic energies (Eqs. (10)–(12)) consist of terms pertaining to the energy transport (i.e., the divergence of the enthalpy, kinetic energy, and Poynting fluxes) and the works done by the pressure gradient and Lorentz forces (W_i^P and W_i^L). Summation of the three energy equations retrieves the law of the total energy conservation expressed in Eq. (3).

The momentum and magnetic flux conservation laws are solved in many numerical schemes that employ the divergence formulation of the MHD equations. However, the internal, kinetic, and magnetic energy equations are not solved as independent equations and, thus, the consistency among them is sometimes violated. In stringent problems, violation of the energy-consistency sometimes yields a negative pressure.

2.2. Discrete operators

This work essentially follows the notation for the finite difference operators given in Morinishi et al. [2]. The finite difference operator with stencil n acting on a variable Φ with respect to x_1 is defined by

$$\frac{\delta_n \Phi}{\delta_n x_1} \equiv \frac{\Phi(x_1 + nh_1/2, x_2, x_3) - \Phi(x_1 - nh_1/2, x_2, x_3)}{nh_1}, \quad (15)$$

where h_1 is the grid spacing in the x_1 -direction. The interpolation operator with stencil n with respect to x_1 is defined as

$$\overline{\Phi}^{nx_1} \equiv \frac{\Phi(x_1 + nh_1/2, x_2, x_3) + \Phi(x_1 - nh_1/2, x_2, x_3)}{2}. \quad (16)$$

In addition, the special interpolation operator of the product of two variables Φ and Ψ with stencil n with respect to x_1 is defined as

$$\begin{aligned} \widetilde{\Phi\Psi}^{nx_1} &\equiv \frac{1}{2} \Phi(x_1 + nh_1/2, x_2, x_3) \Psi(x_1 - nh_1/2, x_2, x_3) \\ &\quad + \frac{1}{2} \Phi(x_1 - nh_1/2, x_2, x_3) \Psi(x_1 + nh_1/2, x_2, x_3). \end{aligned} \quad (17)$$

These operators are similarly defined in the x_2 - and x_3 -directions.

The finite difference operator defined by Eq. (15) is second-order accurate in space. The higher-order finite difference operator can be represented by the weighted average of the n -stencil operator as

$$\frac{\delta \Phi}{\delta x_1} \equiv \sum_{n=1}^{N_c} c_n \frac{\delta_{2n} \Phi}{\delta_{2n} x_1}, \quad (18)$$

where the coefficients c_n satisfy $\sum_n c_n = 1$. For example, the standard five-stencil fourth-order accurate central difference operator ($N_c = 2$, $c_1 = 4/3$, and $c_2 = -1/3$) can be expressed as

$$\frac{\delta \Phi}{\delta x_1} = \frac{4}{3} \frac{\delta_2 \Phi}{\delta_2 x_1} - \frac{1}{3} \frac{\delta_4 \Phi}{\delta_4 x_1}, \quad (19)$$

as shown in Morinishi et al. [2]. These operators are similarly defined in other directions. In Sec. 3.1, two specific implementation of the operator $\delta/\delta x_j$ are provided. We use the operator $\delta/\delta x_j$ as a building block of our formulation to simplify the notation.

The n -stencil finite difference operator satisfies the following three product rules:

$$\Phi \frac{\delta_{2n} \Psi}{\delta_{2n} x_j} + \Psi \frac{\delta_{2n} \Phi}{\delta_{2n} x_j} = \frac{\delta_n \widetilde{\Phi\Psi}^{nx_j}}{\delta_n x_j}, \quad (20)$$

$$\overline{\Phi}^{nx_j} \frac{\delta_n \Psi}{\delta_n x_j} + \overline{\Psi}^{nx_j} \frac{\delta_n \Phi}{\delta_n x_j} = \frac{\delta_n \Phi \Psi}{\delta_n x_j}, \quad (21)$$

and

$$\frac{\overline{\delta_n \Phi}^{nx_j}}{\delta_n x_j} + \Phi \frac{\delta_n \Psi}{\delta_n x_j} = \frac{\delta_n \overline{\Phi}^{nx_j} \Psi}{\delta_n x_j}. \quad (22)$$

The right-hand sides of these equations are conservative. In this study, these product rules are frequently used to analyze the conservation properties of the finite difference scheme. The conservation property of the higher-order operator also satisfies similar relations, such as

$$\Phi \frac{\delta \Psi}{\delta x_j} + \Psi \frac{\delta \Phi}{\delta x_j} = \sum_{n=1}^{N_c} c_n \frac{\delta_n \widetilde{\Phi \Psi}^{nx_j}}{\delta_n x_j}. \quad (23)$$

It is clear that the right-hand side of the equation is conservative.

For future reference, we note the commutation rule of the finite difference operator expressed as

$$\frac{\delta_n}{\delta_n x_i} \left(\frac{\delta_n \Phi}{\delta_n x_j} \right) = \frac{\delta_n}{\delta_n x_j} \left(\frac{\delta_n \Phi}{\delta_n x_i} \right). \quad (24)$$

The higher-order operator also satisfies this rule.

2.3. Energy-consistent formulation of the compressible MHD equations

We propose an energy-consistent formulation of the fully compressible magnetohydrodynamic equations expressed as:

$$\frac{\partial \rho}{\partial t} + \frac{\delta \rho V_j}{\delta x_j} = 0, \quad (25)$$

$$\frac{\partial \rho V_i}{\partial t} + \frac{1}{2} \frac{\delta \rho V_j V_i}{\delta x_j} + \frac{1}{2} \rho V_j \frac{\delta V_i}{\delta x_j} + \frac{1}{2} V_i \frac{\delta \rho V_j}{\delta x_j} = -\frac{\delta P}{\delta x_i} - B_j \left(\frac{\delta B_j}{\delta x_i} - \frac{\delta B_i}{\delta x_j} \right), \quad (26)$$

$$\frac{\partial e}{\partial t} + \frac{\delta (e + P) V_j}{\delta x_j} = V_j \frac{\delta P}{\delta x_j}, \quad (27)$$

$$\frac{\partial B_i}{\partial t} + \frac{\delta (V_j B_i - V_i B_j)}{\delta x_j} = 0. \quad (28)$$

Except the energy equation, the hydrodynamic component of this formulation is similar to the second scheme proposed by Kok [12]. In Kok's scheme, the divergence of the enthalpy flux is expressed using the quadratic split operator. We use the simple divergence form for the enthalpy flux in the internal energy equation for the consistency with the divergence of the mass flux in Eq. (25) and the curl of the electric field in Eqs. (28). One advantage of our formulation is that the pressure perturbation is not excited at the contact discontinuity where P , e , and V_j are constant in space. The energy conservation property is not affected by this change. Note that the entropy conservation can also be achieved by changing the discretization of the equation of the continuity and the internal energy as shown by Kuya et al. [15]. Given that the purpose of this paper is to demonstrate the robustness of the energy-consistent scheme in stringent problems, the details of various formulations for the hydrodynamic equations are not discussed.

2.4. Momentum conservation in the proposed formulation

The convective term in the equations of motion (Eqs. (26)) conserves the volume-averaged momentum as shown in the previous studies [12, 13]. Using the product rule (Eq. (23)), the convective term can be rewritten as

$$\frac{1}{2} \frac{\delta \rho V_j V_i}{\delta x_j} + \frac{1}{2} \rho V_j \frac{\delta V_i}{\delta x_j} + \frac{1}{2} V_i \frac{\delta \rho V_j}{\delta x_j} = \frac{1}{2} \frac{\delta \rho V_j V_i}{\delta x_j} + \sum_{n=1}^{N_c} \frac{c_n}{2} \frac{\widetilde{\delta_n(\rho V_j) V_i}^{nx_j}}{\delta_n x_j}. \quad (29)$$

The right-hand side is conservative, and the convective term conserves momentum.

The Lorentz force in the equations of motion can be also rewritten in the conservative form as

$$F_i^L = -B_j \left(\frac{\delta B_j}{\delta x_i} - \frac{\delta B_i}{\delta x_j} \right) = - \sum_{n=1}^{N_c} c_n \left(\frac{1}{2} \frac{\widetilde{\delta_n B_j B_j}^{nx_i}}{\delta_n x_i} - \frac{\widetilde{\delta_n B_i B_j}^{nx_j}}{\delta_n x_j} \right) - B_i \frac{\delta B_j}{\delta x_j}. \quad (30)$$

The last term disappears when the numerical solenoidal condition

$$\frac{\delta B_j}{\delta x_j} = 0 \quad (31)$$

is satisfied, i.e., the magnetic field divergence is zero.

By removing the $-B_i \nabla \cdot \mathbf{B}$ term in the right-hand side of the momentum equations (see Eq. (8)), an energy-consistent formulation of the MHD equations can be constructed, which conserves momentum even when the numerical solenoidal condition is violated. However, this modification produces artificial forces parallel to the magnetic field lines as well as an additional heating term $V_i B_i \nabla \cdot \mathbf{B}$ in the internal energy equation to maintain the total energy conservation. Therefore, this field-aligned artificial force may yield an unphysical solution. To avoid this problem, the above form of the Lorentz force is selected in this study.

2.5. Total energy conservation in the proposed formulation

This subsection demonstrates the total energy conservation in the proposed formulation. As discussed in previous studies, the skew-symmetric convective term conserves the kinetic energy with the appropriate discretization of the mass conservation law. The convective term multiplied by V_i can be written as

$$\begin{aligned} V_i \left[\frac{1}{2} \frac{\delta \rho V_j V_i}{\delta x_j} + \frac{1}{2} \rho V_j \frac{\delta V_i}{\delta x_j} + \frac{1}{2} V_i \frac{\delta \rho V_j}{\delta x_j} \right] &= \frac{1}{2} V_i \frac{\delta \rho V_j V_i}{\delta x_j} + \frac{1}{2} \rho V_j V_i \frac{\delta V_i}{\delta x_j} + \frac{V_i V_i}{2} \frac{\delta \rho V_j}{\delta x_j} \\ &= \sum_{n=1}^{N_c} \frac{c_n}{2} \frac{\widetilde{\delta_n(\rho V_j V_i) V_i}^{nx_j}}{\delta_n x_j} + \frac{V_i V_i}{2} \frac{\delta \rho V_j}{\delta x_j}. \end{aligned} \quad (32)$$

The kinetic energy equation is derived from the equations of motion Eqs. (26) and the equation of continuity Eq. (25) as

$$\begin{aligned} \frac{\partial \rho V_i V_i / 2}{\partial t} &= V_i \frac{\partial \rho V_i}{\partial t} - \frac{V_i V_i}{2} \frac{\partial \rho}{\partial t} \\ &= - \sum_{n=1}^{N_c} \frac{c_n}{2} \frac{\delta_n(\rho V_j V_i) V_i}{\delta_n x_j} + W^P + W^L. \end{aligned} \quad (33)$$

The first term of the last equation represents the divergence of the kinetic energy flux. The second term of Eq. (32) is canceled with the equation of continuity.

The work done by the pressure gradient force

$$W^P = -V_j \frac{\delta P}{\delta x_j} \quad (34)$$

represents the interaction between the internal and kinetic energy equations. Apparently, this is exactly equivalent to the right-hand side of the internal energy equation Eq. (27), apart from the difference in sign.

The magnetic energy equation is derived by multiplying the induction equation Eq. (28) by B_i , such that

$$\begin{aligned} \frac{\partial B_i B_i / 2}{\partial t} &= B_i \frac{\partial B_i}{\partial t} = -B_i \frac{\delta(V_j B_i - V_i B_j)}{\delta x_j} \\ &= - \sum_{n=1}^{N_c} c_n \frac{\delta_n B_i (V_j B_i - V_i B_j)}{\delta_n x_i} - W^L, \end{aligned} \quad (35)$$

where the first term in the last equation is (minus of) the divergence of the Poynting flux and the second term represents the work done by the Lorentz force

$$W^L = -V_i B_j \left(\frac{\delta B_j}{\delta x_i} - \frac{\delta B_i}{\delta x_j} \right). \quad (36)$$

Comparison with the discretized Lorentz force of Eq. (30) reveals that the interaction between the kinetic and magnetic energy equations is consistent in the discretization level. Note that we did not use the solenoidal condition of Eq. (31) in the derivation of the magnetic energy equation. Thus, the proposed formulation conserves the total energy even when the $\nabla \cdot \mathbf{B} = 0$ condition is violated.

2.6. Energy-consistent formulation of the nonlinear filtering flux

Shock waves and discontinuities are often involved in the solutions of compressible hydrodynamics and magnetohydrodynamics. In the approach adopted in this work, the numerical simulation is stabilized by diffusing the sharp gradient through introducing of the nonlinear filtering flux in the semi-discrete formulation of Eqs. (25)–(28). An energy-consistent formulation is obtained even when this nonlinear filtering flux is introduced.

We design an energy-consistent formulation for the filtering flux defined at the center of the cell face. Note that many linear and nonlinear filtering schemes can be reduced to this formulation. The filtering process of the variable U can be expressed as

$$\frac{\partial U}{\partial t} = \frac{\delta_1 D_j(U)}{\delta_1 x_j}, \quad (37)$$

where $D_j(U)$ is the filtering flux in the j -th direction defined at the cell edge. The typical first-order filtering flux can be expressed as

$$D_j(U) = \eta(U) \frac{\delta_1 U}{\delta_1 x_j}, \quad (38)$$

where $\eta(U)$ is the diffusion coefficient of U . The construction of the higher-order filtering flux is described in Section 3. The energy-consistent property is not affected by the specific implementation of the filtering flux $D_j(U)$ as long as the filtering flux is defined at the cell face. In this study, we apply this filtering scheme on the mass density ρ , the momentum density ρV_i , the magnetic flux density B_i , and the internal energy density e .

When the filtering scheme is applied on the equations of motion or the induction equations, the viscous heating Q_{vis} or the resistive heating Q_{res} should be included as heating terms in the internal energy equation to maintain the total energy conservation. We propose the energy-consistent discretization of the viscous and resistive heating rates corresponding to the filtering flux as

$$Q_{\text{vis}} = \overline{D_j(\rho V_i) \frac{\delta_1 V_i}{\delta_1 x_j}}^{1x_j} - \frac{\overline{D_j(\rho)} \delta_1 V_i V_i}{2 \delta_1 x_j}^{1x_j} \quad (39)$$

and

$$Q_{\text{res}} = \overline{D_j(B_i) \frac{\delta_1 B_i}{\delta_1 x_j}}^{1x_j}, \quad (40)$$

respectively. These expressions can be rewritten as

$$Q_{\text{vis}} = \frac{\delta_1}{\delta_1 x_j} \left[\overline{V_i}^{1x_j} D_j(\rho V_i) - \frac{1}{2} \overline{V_i V_i}^{1x_j} D_j(\rho) \right] - V_i \frac{\delta_1 D_j(\rho V_i)}{\delta_1 x_j} + \frac{V_i V_i}{2} \frac{\delta_1 D_j(\rho)}{\delta_1 x_j} \quad (41)$$

and

$$Q_{\text{res}} = \frac{\delta_1 \overline{B_i}^{1x_j} D_j(B_i)}{\delta_1 x_j} - B_i \frac{\delta_1 D_j(B_i)}{\delta_1 x_j}. \quad (42)$$

Here, the first terms in these two equations are the kinetic and magnetic energy transport by the filtering fluxes, respectively. The other terms correspond to the time variation of the kinetic and magnetic energies produced by the filtering flux. Clearly, these heating rates are energy-consistent in terms of the exchange among the internal, kinetic, and magnetic energies.

The viscous and resistive heating rates defined in Eqs. (39) and (40) become positive under the specific condition. We assume the filtering flux of the momentum density ρV_i evaluated from those of the mass density and velocity field as

$$D_j(\rho V_i) = \overline{\rho}^{1x_j} D_j(V_i) + \overline{V_i}^{1x_j} D_j(\rho). \quad (43)$$

Then, the viscous heating rate Eq. (39) can be rewritten as

$$Q_{\text{vis}} = \overline{\left[\overline{\rho}^{1x_j} D_j(V_i) + \overline{V_i}^{1x_j} D_j(\rho) \right] \frac{\delta_1 V_i}{\delta_1 x_j}} - \frac{\overline{D_j(\rho) \delta_1 V_i V_i}^{1x_j}}{2 \delta_1 x_j} = \overline{\rho}^{1x_j} D_j(V_i) \frac{\delta_1 V_i}{\delta_1 x_j}, \quad (44)$$

where the product rule of Eq. (21) for $\Phi = \Psi = V_i$ is used. The above viscous heating rate becomes positive if the sign of $D_j(V_i)$ is the same as that of $\delta_1 V_i / \delta_1 x_j$. This condition is often satisfied considering that the $D_j(V_i)$ is the filtering flux acting to diffuse V_i in the x_j -direction. Similarly, the resistive heating rate Eq. (40) becomes positive when $D_j(B_i)$ and $\delta_1 B_i / \delta_1 x_j$ have the same sign.

2.7. Treatment of magnetic monopole

In the multi-dimensional simulations of the magnetohydrodynamics, the solenoidal condition $\nabla \cdot \mathbf{B} = 0$ should be preserved throughout the time integration. Violating the solenoidal rule may produce artificial inconsistencies in the numerical solution.

The central difference scheme is known to produce no numerical magnetic monopole [23] as

$$\begin{aligned} \frac{\delta}{\delta x_i} \left(\frac{\partial B_i}{\partial t} \right) &= -\frac{\delta}{\delta x_i} \left[\frac{\delta (V_j B_i - V_i B_j)}{\delta x_j} \right] \\ &= -\frac{\delta}{\delta x_i} \left(\frac{\delta V_j B_i}{\delta x_j} \right) + \frac{\delta}{\delta x_i} \left(\frac{\delta V_i B_j}{\delta x_j} \right) \\ &= 0. \end{aligned} \quad (45)$$

Here, we use the commutation rule of the central difference operators (Eq. (24)). On the other hand, the filtering flux violates the solenoidal condition $\nabla \cdot \mathbf{B} = 0$ as

$$\frac{\delta}{\delta x_k} \left[\frac{\delta_1 D_j(B_i)}{\delta_1 x_j} \right] \neq 0. \quad (46)$$

We need some treatment to control the magnetic monopole on the numerical solution.

In this study, the hyperbolic/parabolic divergence cleaning method [24] is used to control the divergence of the magnetic field. The numerical magnetic monopole is transported and diffused by introducing an additional equation of the generalized Lagrange multiplier (GLM) ψ as

$$\frac{\partial \psi}{\partial t} = -c_\psi^2 \frac{\delta B_i}{\delta x_i} - \frac{\psi}{\tau_\psi}, \quad (47)$$

where the propagation speed c_ψ and the damping rate τ_ψ are the tunable parameters that control the efficiency of the divergence cleaning. Correspondingly, the induction equations are corrected as

$$\frac{\partial B_i}{\partial t} = -\frac{\delta\psi}{\delta x_i}, \quad (48)$$

where, for the sake of clarity, we dropped the terms containing the curl of the electric field and the filtering flux on the magnetic flux density. It is clear that the divergence cleaning method conserves the magnetic flux in a volume.

Although the hyperbolic/parabolic divergence cleaning method can efficiently reduce the divergence of the magnetic field, $\nabla \cdot \mathbf{B}$ still remains in the numerical solution. The numerical discretization should be energy-consistent even when the small numerical error of $\nabla \cdot \mathbf{B}$ exists. This method produces the additional term in the magnetic energy equation as

$$\frac{\partial B_i^2/2}{\partial t} = -B_i \frac{\delta\psi}{\delta x_i} = -\sum_{n=1}^{N_c} c_n \frac{\widetilde{\delta_n B_i \psi}^{nx_i}}{\delta_n x_i} - Q_\psi, \quad (49)$$

where we define the heating term due to the divergence cleaning method

$$Q_\psi = -\psi \frac{\delta B_i}{\delta x_i}. \quad (50)$$

In the steady state, this term becomes positive, as

$$Q_\psi \rightarrow \tau_\psi c_\psi^2 \left(\frac{\delta B_i}{\delta x_i} \right)^2 \geq 0. \quad (51)$$

Introduction of Q_ψ in the internal energy equation provides the energy-consistent formulation with the hyperbolic/parabolic divergence cleaning.

2.8. Summary of the proposed scheme

The energy-consistent formulation of the compressible MHD equations is summarized as follows:

$$\frac{\partial \rho}{\partial t} + \frac{\delta \rho V_j}{\delta x_j} = \frac{\delta_1 D_j(\rho)}{\delta_1 x_j}, \quad (52)$$

$$\frac{\partial \rho V_i}{\partial t} + \frac{1}{2} \frac{\delta \rho V_j V_i}{\delta x_j} + \frac{1}{2} \rho V_j \frac{\delta V_i}{\delta x_j} + \frac{1}{2} V_i \frac{\delta \rho V_j}{\delta x_j} + \frac{\delta P}{\delta x_i} + B_j \frac{\delta B_j}{\delta x_i} - B_j \frac{\delta B_i}{\delta x_j} = \frac{\delta_1 D_j(\rho V_i)}{\delta_1 x_j}, \quad (53)$$

$$\frac{\partial e}{\partial t} + \frac{\delta(e+P)V_j}{\delta x_j} = -V_j \frac{\delta P}{\delta x_j} + \frac{\delta_1 D_j(e)}{\delta_1 x_j} + Q_{\text{vis}} + Q_{\text{res}} + Q_\psi, \quad (54)$$

$$\frac{\partial B_i}{\partial t} + \frac{\delta(V_j B_i - V_i B_j)}{\delta x_j} + \frac{\delta\psi}{\delta x_i} = \frac{\delta_1 D_j(B_i)}{\delta_1 x_j}, \quad (55)$$

$$\frac{\partial \psi}{\partial t} + c_\psi^2 \frac{\delta B_j}{\delta x_j} = -\frac{\psi}{\tau_\psi} + \frac{\delta_1 D_j(\psi)}{\delta_1 x_j}. \quad (56)$$

The viscous and resistive heating rates (Q_{vis} and Q_{res}) are defined in Eqs. (39) and (40), respectively. The heating caused by the numerical magnetic monopole Q_ψ is defined in Eq. (50). In this formulation, the internal, kinetic, and magnetic energy equations are consistent even if the nonlinear filtering flux and the divergence cleaning are introduced. The energy-consistent formulation of the compressible hydrodynamic equations can be derived by setting B_i , ψ , Q_{res} , and Q_ψ to be zero in Eqs. (52)–(54). The proposed formulation is independent of the specific implementations of the temporal discretization, the central difference operator $\delta/\delta x_j$, and the nonlinear filtering flux $D_j(U)$ for each variable U . The details of our implementation are described in Section 3.

3. Numerical implementation

This section describes the details of our implementation of the proposed formulation. In the proposed formulation Eqs. (52)–(56), the time derivative is not discretized.

3.1. Base schemes for scalar advection equation

In this subsection, we describe our implementation and performance of the base schemes using the one-dimensional scalar advection equation:

$$\frac{\partial U}{\partial t} + a \frac{\partial U}{\partial x_1} = 0, \quad (57)$$

where U is the scalar variable and a is the advection speed. The semi-discrete form of the above equation can be written as

$$\frac{\partial U}{\partial t} + a \frac{\delta U}{\delta x_1} = \frac{\delta_1 D_1(U)}{\delta_1 x_1}. \quad (58)$$

We implemented the second- and fifth-order schemes to show the general performance of the proposed formulation. The important feature of these schemes is the small numerical overshoot, which seems to contribute the high robustness of our formulation shown in Sec. 4. We speculate that the similar high robustness can be achieved with other combination of the central difference operator and filtering flux, as long as the produced numerical overshoot is sufficiently small.

In the second-order scheme, we used the second-order central difference operator $\delta/\delta x_j$ defined in Eq. (18) by setting $N_c = 1$ and $c_1 = 1$. The second-order filtering flux was taken from the Jameson-Schmidt-Turkel (JST) scheme [7, 25]. The JST scheme is total variation diminishing if the limiter function is chosen appropriately [26]. Among the variant of the JST scheme, we used the symmetric limited positive (SLIP) scheme [27], which is proven to be positivity preserving for the scalar conservation law. The filtering flux of the SLIP scheme for the scalar advection equation can be written as

$$D_1^{\text{JST}}(U; x_1 + h_1/2) = \frac{|a|}{2} [\Delta U_{x_1+h_1/2} - \mathcal{L}(\Delta U_{x_1+3h_1/2}, \Delta U_{x_1-h_1/2})], \quad (59)$$

where $\Delta U_x = U(x + h_1/2) - U(x - h_1/2)$ is the difference of U between two adjacent cells and $\mathcal{L}(a, b)$ is the limiter function. We used van Leer's limiter (originally introduced in [28], implemented as described by [27]) for the limiter function \mathcal{L} .

To demonstrate the applicability of the proposed scheme in the higher order, we also implemented the fifth-order scheme using the sixth-order central difference operator $\delta/\delta x_j$ for $N_c = 3$, $c_1 = 3/2$, $c_2 = -3/5$, and $c_3 = 1/10$. The filtering flux is based on the fifth-order weighted essentially non-oscillatory (WENO) reconstruction [29]. The WENO scheme was originally developed in the context of the upwind scheme and is not intended to be used as the filtering flux for the central difference method. The filtering flux in the x_1 -direction based on the WENO reconstruction can be written as

$$D_1^{\text{WENO}}(U; x_1 + h_1/2) = \frac{c_{\text{diff}} |a|}{2} [U^{\text{R}}(x_1 + h_1/2) - U^{\text{L}}(x_1 + h_1/2)], \quad (60)$$

where U^{R} and U^{L} are the upwind value of U reconstructed from the positive and negative x_1 -direction, respectively. A positive diffusion parameter c_{diff} of order unity is introduced to control the numerical diffusion by the filtering flux.

The one-dimensional scalar advection equation Eq. (57) conserves its energy $U^2/2$ as

$$\frac{\partial U^2/2}{\partial t} + a \frac{\partial U^2/2}{\partial x_1} = 0. \quad (61)$$

The corresponding semi-discrete equation can be obtained by multiplying Eq. (58) by U as

$$U \frac{\partial U}{\partial t} + a \left(\sum_{n=1}^{N_c} c_n \frac{\widetilde{\delta_n U^2/2}^{nx_1}}{\delta_n x_1} \right) - \frac{\delta_1 \bar{U}^{1x_1} D_1(U)}{\delta_1 x_1} = -D_1(U) \frac{\delta_1 U^{1x_1}}{\delta_1 x_1}, \quad (62)$$

where the right-hand side represents the energy loss by the filtering flux $D_1(U)$. Note that the similar terms of the energy loss in the kinetic and magnetic energy equations in our MHD formulation are treated as the viscous and resistive heating rates in the internal energy equation to achieve the total energy conservation even if the filtering flux is introduced (see Sec. 2.6). The semi-discrete scheme Eq. (58) conserves the energy $U^2/2$ if the energy loss by the filtering flux is negligible. However, the temporal discretization can violate the energy conservation because the analytical identity $U \partial U / \partial t = \partial(U^2/2) / \partial t$ cannot be satisfied by a time integration scheme in general, like most of the Runge-Kutta methods. One simple exception is the implicit midpoint method, which is symmetric in temporal direction. Similar to the advection equation, the total energy conservation in the semi-discrete formulation of the MHD equations in Eqs. (52)–(56) produces the conservation error of the total energy by the time integration scheme. More detailed descriptions on the relation between the energy conservation and the temporal integration method can be found in [12, 13].

In all test problems described in this paper, we used the third-order optimal strongly stability preserving (SSP) Runge-Kutta method [30] for the SSP property in the nonlinear equations [31] and its frequent use with the fifth-order WENO scheme [29]. We also found that the four-step second-order Runge-Kutta method by Jameson & Baker [32] also performs

well even in the stringent problems in Secs. 4.5 and 4.6. Therefore, we speculate that the robustness of the proposed formulation may be weakly affected by the choice of the time integration scheme.

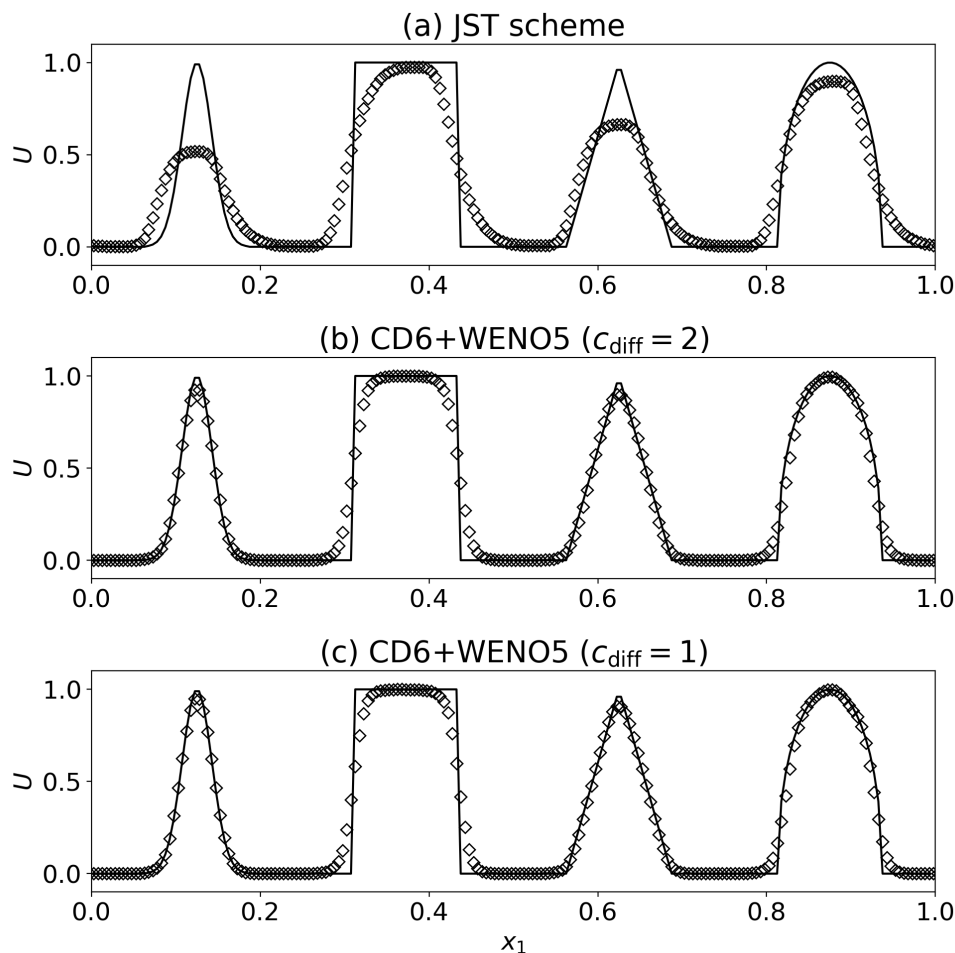


Figure 1: Results of one-dimensional scalar advection problem using 200 grid points. Shown are the results at $t = 1$ for (a) JST scheme, (b) sixth-order central difference method with the filtering flux by the WENO5 scheme with $c_{\text{diff}} = 2$, and (c) sixth-order central difference method with the filtering flux by the WENO5 scheme with $c_{\text{diff}} = 1$. The solid lines indicate the analytical solution. The diamond symbols indicate the numerical results. The Courant number of 0.3 is used.

Figure 1 shows the solution of the one-dimensional scalar advection problem after one period. The initial profile is identical to that of the test problem in Suresh & Huynh [33]. The results show that both the second-order scheme with the JST filtering flux and the sixth-order scheme with the fifth-order WENO filtering flux efficiently preserve the monotonicity of the solution.

The dependence on the diffusion parameter c_{diff} of the WENO filter becomes clear near the discontinuity. Figure 2 shows solutions for the same problem as Fig. 1, but showing

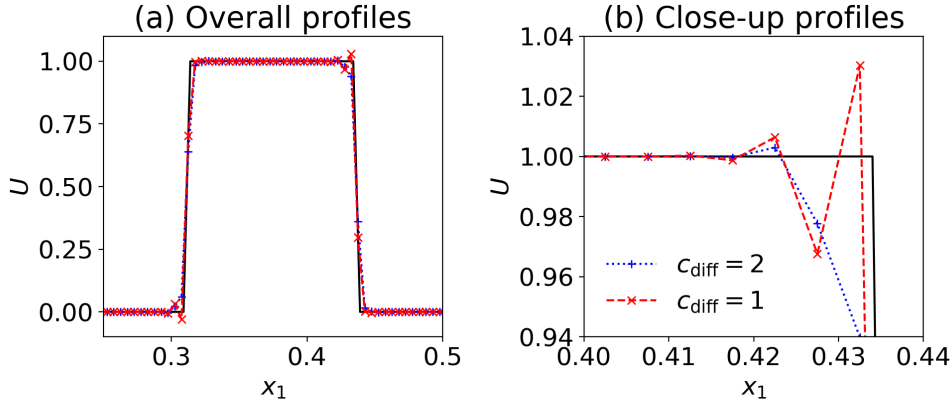


Figure 2: One-dimensional scalar advection problem using 200 grid points with sixth-order central difference method with the filtering flux by the WENO5 scheme. Shown are the results one step after the integration (at $t = 0.0015$) for $c_{\text{diff}} = 2$ (blue dotted lines with plus) and $c_{\text{diff}} = 1$ (red dashed lines with cross). The solid lines indicate the analytical solution. The Courant number of 0.3 is used.

one step after the time integration (at $t = 0.0015$). Small numerical overshoots are found near the discontinuity if $c_{\text{diff}} = 1$. We found that the overshoot can be efficiently damped by doubling the numerical diffusion in the WENO filter ($c_{\text{diff}} = 2$). However, small overshoot of about 10^{-5} still remains even if $c_{\text{diff}} = 2$. We note that this value of $c_{\text{diff}} = 2$ is not guaranteed theoretically nor optimized for general problems. However, this choice was found to show high numerical stability in all test problems presented in Sec. 4. Because the formulation proposed in this study is independent of the specific implementation of the filtering flux, better methods of evaluating the filtering flux, especially with less numerical overshoot and higher-order spatial convergence, should be investigated in future studies.

3.2. Filtering flux for system equations

For the primitive variables in the MHD equations with the hyperbolic/parabolic divergence cleaning method, $W_i = (\rho, e, V_1, V_2, V_3, B_1, B_2, B_3, \psi)$, the one-dimensional form of the evolution equations can be written as

$$\frac{\partial W_l}{\partial t} + \sum_n A_{ln} \frac{\partial W_n}{\partial x_1} = 0, \quad (63)$$

where A is the coefficient matrix for the primitive variables. The matrix A can be diagonalized as

$$A_{ln} = \sum_m R_{lm} \lambda_m L_{mn}, \quad (64)$$

where L and R are the left and right eigenmatrices [34, 35], respectively, and λ_m indicates the eigenvalues of the matrix A .

There are several ways to extend the filtering flux for the scalar advection equation to the system equations. Here, we implemented two methods, namely, the LLF-type and the

Roe-type filtering schemes. The first approach to evaluate the filtering flux is to diffuse all variables with the same characteristic speed, as in the local Lax-Friedrichs (LLF) scheme [36, 37]. The filtering flux of the primitive variables in the x_1 -direction at the location $x_1 + h_1/2$ is computed as

$$D(W_i; x_1 + h_1/2) = \frac{a_{\max}}{2} \mathcal{D} [W(x_1 + h_1/2 \pm h_1/2), W(x_1 + h_1/2 \pm 3h_1/2), \dots], \quad (65)$$

where $a_{\max} = \max(|\lambda_1|, \dots, |\lambda_9|)$ is the maximum phase speed of the waves in the system and the discrete operator \mathcal{D} represents the limiting process in the JST and WENO5 filtering fluxes. The filtering flux for the momentum density was computed from that of the mass density and the velocity field using Eq. (43).

The second filtering flux implemented in this study is based on Roe's approximate Riemann solver [38, 26, 16], which is given by

$$D(W_i; x_1 + h_1/2) = \frac{1}{2} \sum_m R_{lm} |\lambda_m| \mathcal{D} [Q_m(x_1 + h_1/2 \pm h_1/2), Q_m(x_1 + h_1/2 \pm 3h_1/2), \dots], \quad (66)$$

where

$$Q_m(x_1) = \sum_n L_{mn} W_n(x_1) \quad (67)$$

is the characteristic variables with the phase speed of λ_m . The left and right eigenmatrices R_{ij} and L_{jk} and the eigenvalues λ_j are evaluated at the fixed location $x_1 + h_1/2$. In our implementation, these eigenmatrices and eigenvalues are derived from the arithmetic average of the primitive variables at the adjacent grids, i.e., $\overline{W_i}^{1x_1}(x_1 + h_1/2) = (W_i(x_1) + W_i(x_1 + h_1))/2$. Although the original Roe's scheme [38] employs the Roe-average, the arithmetic average has often been utilized in practical problems, and it seems to work well [39]. We also used the first entropy fix suggested by Harten & Hyman [40] to evaluate the eigenvalues. The filtering flux of the momentum density was derived using Eq. (43).

In the Roe-type method, the characteristic variables are used for the filtered variables instead of the primitive variables to improve the monotonicity of the numerical solution [41]. The positivity of the viscous and resistive heating rates discussed in Sec. 2.6 may be violated when the Roe-type method is applied. We actually found that the Roe-type method provides less robustness than the LLF-type method when the internal energy is much smaller than the kinetic or magnetic energy.

3.3. Time step size and parameters of hyperbolic/parabolic divergence cleaning method

The time step size Δt is determined from the Courant-Friedrichs-Lewy (CFL) condition

$$\Delta t = \min_{x_1, x_2, x_3} \left\{ \sigma_{\text{CFL}} \left[\sum_{i=1}^{N_D} \frac{\max(|\lambda_{i,2}(x_1, x_2, x_3)|, |\lambda_{i,8}(x_1, x_2, x_3)|)}{h_i} \right]^{-1} \right\}, \quad (68)$$

where $\lambda_{i,2}$ and $\lambda_{i,8}$ are the eigenvalues for the fast magneto-acoustic waves calculated for the x_i -direction, σ_{CFL} is the Courant number of order unity, and $N_D = 1, 2, 3$ is the number of

dimensions. In the most test problems shown in Sec. 4, we set the default Courant number $\sigma_{\text{CFL}} = 0.3$. Although most problems can be solved with larger σ_{CFL} like 0.4 or 0.5, the value of 0.3 is required for stability in the stringent problems described in Secs. 4.5 and 4.6.

In the multi-dimensional problems, we used the hyperbolic/parabolic divergence cleaning method. The propagation speed of the magnetic field divergence c_ψ is computed from the CFL condition at each time step as

$$c_\psi = \sigma_{\text{CFL}} \left[\Delta t \sum_{i=1}^{N_D} \frac{1}{h_i} \right]^{-1}. \quad (69)$$

The damping time τ_ψ was set to $10\Delta t$. More detailed discussion on the choice of the damping time τ_ψ can be found in [24, 42].

4. Test problems

Based on the newly proposed formulation described in Sec. 2.8, four schemes were implemented, namely, JST-LLF, JST-Roe, WENO5-LLF, and WENO5-Roe schemes. In the JST-LLF and JST-Roe schemes, the second-order central difference with the filtering flux based on the SLIP version of the Jameson-Schmidt-Turkel scheme was used. In the two WENO5 schemes, the sixth-order central difference with the filtering flux based on the fifth-order WENO reconstruction is used. The JST-LLF and WENO5-LLF schemes are based on the LLF-type filtering scheme, and the JST-Roe and WENO5-Roe schemes are implemented with the Roe-type filtering scheme. See Section 3 for the details of our implementation. We found that the LLF-type filtering scheme becomes more numerically robust than the Roe-type scheme. Most of the test problems presented in this study can be solved with both the LLF- and Roe-type filtering schemes, unless otherwise noted. The exceptions are the most stringent, non-standard test problems described in Secs. 4.5 and 4.6.

All four schemes were integrated using the three-step third-order optimal SSP Runge–Kutta method [43]. The Courant number σ_{CFL} of 0.3 was used in all test problems, unless otherwise noted. The equation of states of ideal gas was used in all problems.

4.1. Two-dimensional magnetized iso-density vortex problem

We analyze the spatial accuracy of the four proposed schemes (JST-LLF, JST-Roe, WENO5-LLF, and WENO5-Roe) using the magnetized iso-density vortex problem proposed by Balsara [44]. As argued in [45], the Gaussian taper of variables in the original problem produces a small error near the boundary, which may reduce the convergence rate of higher-order schemes. To avoid this effect, we chose a version of this problem described in Mignone et al. [42]. The initial condition is described by $\rho = 1$, $(V_1, V_2) = (1, 1) + (-x_2, x_1)\kappa e^{q(1-r^2)}$, $(B_1, B_2) = (-x_2, x_1)\mu e^{q(1-r^2)}$, and $p = 1 + [\mu^2(1 - qr^2) - \kappa^2\rho]e^{2q(1-r^2)}/(4q)$, where $r = \sqrt{x_1^2 + x_2^2}$, $\kappa = 1/(2\pi)$, and $\mu = 1/(2\pi)$. In the actual implementation, we use the magnetic vector potential $A_3 = \mu e^{q(1-r^2)}/(2q)$ to compute the magnetic field as $(B_1, B_2) = (\delta A_3/\delta x_2, -\delta A_3/\delta x_1)$ so that the discretization error of $\nabla \cdot \mathbf{B}$ becomes zero in the initial

Table 1: L_1 norm errors and corresponding convergence rates for the two-dimensional magnetized iso-density vortex problem. The errors are measured in the x_1 -component of the magnetic field B_1 and the divergence of the magnetic field $\nabla \cdot \mathbf{B}$. Note that we set $q = 0.5$ for the second-order schemes (JST-Roe, JST-LLF, and CD2) and $q = 1.0$ for the higher-order schemes (WENO5-Roe, WENO5-LLF, and CD6).

Method	Number of mesh	L_1 error of B_1	L_1 order of B_1	L_1 error of $\nabla \cdot \mathbf{B}$	L_1 order of $\nabla \cdot \mathbf{B}$
JST-LLF	32×32	1.0526×10^{-2}		4.0819×10^{-4}	
	64×64	5.1003×10^{-3}	1.05	4.1512×10^{-4}	-0.02
	128×128	1.5464×10^{-3}	1.72	1.8711×10^{-4}	1.15
	256×256	4.4229×10^{-4}	1.81	4.3809×10^{-5}	2.09
JST-Roe	32×32	7.7712×10^{-3}		5.2883×10^{-4}	
	64×64	2.9609×10^{-3}	1.39	4.2245×10^{-4}	0.32
	128×128	9.2047×10^{-4}	1.69	1.5609×10^{-4}	1.44
	256×256	2.7493×10^{-4}	1.74	3.8375×10^{-5}	2.02
CD2	32×32	7.9730×10^{-3}		1.2133×10^{-17}	
	64×64	2.0322×10^{-3}	1.97	1.9345×10^{-17}	
	128×128	5.1359×10^{-4}	1.98	3.7870×10^{-17}	
	256×256	1.2875×10^{-4}	2.00	7.4208×10^{-17}	
WENO5-LLF	32×32	4.3520×10^{-3}		9.5700×10^{-5}	
	64×64	5.2244×10^{-4}	3.06	2.2263×10^{-5}	2.10
	128×128	3.0996×10^{-5}	4.08	8.8323×10^{-7}	4.66
	256×256	1.5011×10^{-6}	4.37	3.4229×10^{-8}	4.69
WENO5-Roe	32×32	2.9596×10^{-3}		8.9004×10^{-5}	
	64×64	2.6993×10^{-4}	3.45	1.7274×10^{-5}	2.37
	128×128	1.5427×10^{-5}	4.13	6.7352×10^{-7}	4.68
	256×256	6.8663×10^{-7}	4.49	2.6719×10^{-8}	4.66
CD6	32×32	6.3801×10^{-4}		1.1525×10^{-17}	
	64×64	1.0654×10^{-5}	5.90	2.4753×10^{-17}	
	128×128	1.7796×10^{-7}	5.90	5.8132×10^{-17}	
	256×256	4.9065×10^{-9}	5.18	2.0371×10^{-16}	

condition. The simulation evolves over a time of 10 units in the two-dimensional domain of $[-5, 5] \times [-5, 5]$ with periodic boundary conditions. Following [42], we set $q = 0.5$ for the second-order schemes (JST-LLF and JST-Roe) and $q = 1.0$ for the fifth-order schemes (WENO5-LLF and WENO5-Roe). We used the Courant number $\sigma_{\text{CFL}} = 0.3$ in all cases.

Table 1 summarizes the L_1 errors and corresponding convergence rates measured in B_1 and $\nabla \cdot \mathbf{B}$. The L_1 error of a quantity U is computed as an average of the absolute value of the difference between the initial and final solutions over the whole domain. All schemes converge to the designed order of accuracy in both B_1 and $\nabla \cdot \mathbf{B}$. The errors and convergence rates of the magnetic field B_1 can be directly compared to Table 3 of [42]. As expected, our second-order schemes provide larger errors than the third-order schemes described in [42]. The errors and convergence rates by the second-order total variation diminishing scheme in Table 5 of [44] seems to be comparable or slightly worse than our JST-LLF scheme. Our fifth-order schemes also provides larger L_1 errors than the fifth-order schemes in [42]. This difference is caused by the larger numerical diffusion by the enhancement of the filtering flux (by setting $c_{\text{diff}} = 2$) and the less diffusive reconstruction by WENO-Z [46] or MP5 [33]

schemes used in [42].

For comparison, we also show the results of two additional central difference schemes CD2 and CD6 in Table 1. The CD2 and CD6 schemes are the second- and sixth-order central difference schemes derived by setting the filtering flux to be zero in the JST and WENO5 schemes. The convergence rates of these central schemes are independent from the filtering scheme and the numerical divergence of the magnetic field. Both schemes are less diffusive and rapidly converge to the designed order of accuracy. As the amount of $\nabla \cdot \mathbf{B}$ produced by the central difference schemes (CD2 and CD6) is limited by the machine epsilon of the floating-point operation, the order of convergence for $\nabla \cdot \mathbf{B}$ is not shown. The slight reduction in the convergence rate between 128×128 and 256×256 grid points in the CD6 scheme is caused by the third-order error of the time integration scheme. If we compute the case of 256×256 grid points of the CD6 scheme with smaller CFL number of 0.075, the L_1 error and convergence rate of B_1 is 2.7752×10^{-9} and 6.00, respectively.

4.2. One-dimensional hydrodynamic shock tube problems

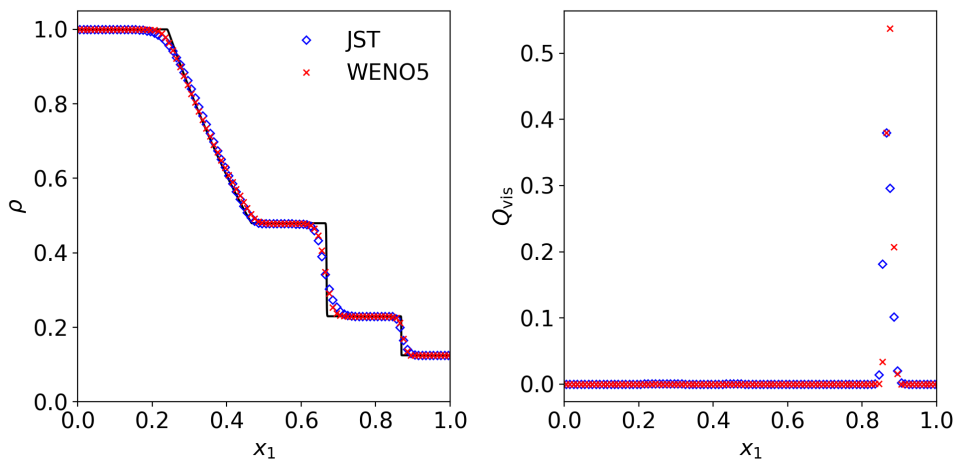


Figure 3: One-dimensional Sod’s shock tube problem using 100 grid points. Shown are the mass density (left panel) and the viscous heating rate (right panel) at $t = 0.2$ for the JST-Roe scheme (blue diamond) and the WENO5-Roe scheme (red cross). The solid lines indicate the reference solution calculated with the WENO5-Roe scheme using 4000 grid points.

The hydrodynamic Sod’s shock tube problem [47] is used to measure the performance of the proposed schemes near the shock wave and discontinuity. Figure 3 shows the one-dimensional simulation of the Sod’s problem calculated with 100 grid points. The proposed schemes (JST-Roe and WENO5-Roe) successfully captured the shock front, contact discontinuity, and rarefaction wave. One advantage of the proposed scheme is that the numerical viscous heating can be derived explicitly. The result indicates that the viscous heating was concentrated near the shock front near $x \sim 0.9$, with a positive sign indicating the heating process. The viscous heating was negligible at the contact discontinuity or rarefaction wave.

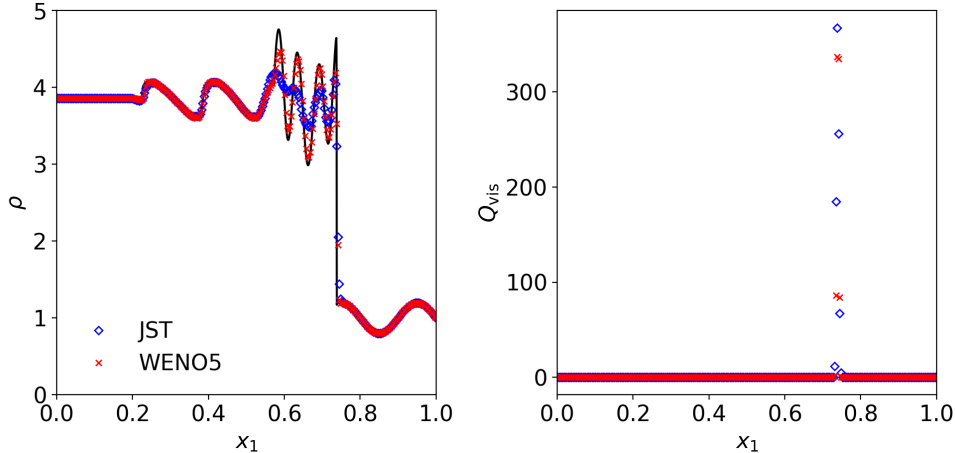


Figure 4: One-dimensional Shu–Osher’s shock tube problem using 300 grid points. Shown are the mass density (left panel) and the viscous heating rate (right panel) at $t = 0.18$ for the JST-Roe scheme (blue diamond) and the WENO5-Roe scheme (red cross). The solid lines indicate the reference solution calculated with the WENO5-Roe scheme using 4000 grid points.

The advantage of the higher-order scheme can be apparent in the Shu–Osher’s shock tube problem [43]. Figure 4 shows the results of the one-dimensional Shu-Osher’s test using 300 grid points. The higher-order WENO5-Roe scheme could resolve the wavy pattern after the shock front better than the JST-Roe scheme. The viscous heating is concentrated near the shock front at $x \sim 0.7$.

4.3. One-dimensional MHD shock tube problems

In the one-dimensional MHD test problems, the discretization error of the magnetic field divergence becomes zero. Thus, we can assess the performance of the proposed schemes without the influence of the $\nabla \cdot \mathbf{B}$ error.

The Dai–Woodward’s MHD shock tube problem [48] involves various shock waves and discontinuities (i.e., the fast shocks, rotational discontinuities, and slow shocks propagating from each side of the contact discontinuity). Figure 5 shows the results of the one-dimensional Dai-Woodward shock tube problem with 200 grid points. The JST-Roe and WENO5-Roe schemes were sufficiently robust and captured all shocks and discontinuities in this problem. No visible numerical overshoots were observed. The viscous and resistive heating rates are prominently located near the two fast shock fronts.

The second MHD shock tube problem considered in this study is the MHD analog of the Sod’s shock tube problem originally introduced by Brio & Wu [49], with the specific heat ratio $\gamma = 2$. Our test problem is a variant of this problem with $\gamma = 5/3$ presented by Ryu & Jones [39]. The numerical solution obtained with 200 grid points is shown in Figure 6. This problem involves so-called slow compound shock located near $x \sim 0.5$. The numerical solutions calculated with both the JST-Roe and WENO5-Roe schemes agree well with the previously reported results. Most of the viscous and resistive heating rates appeared near

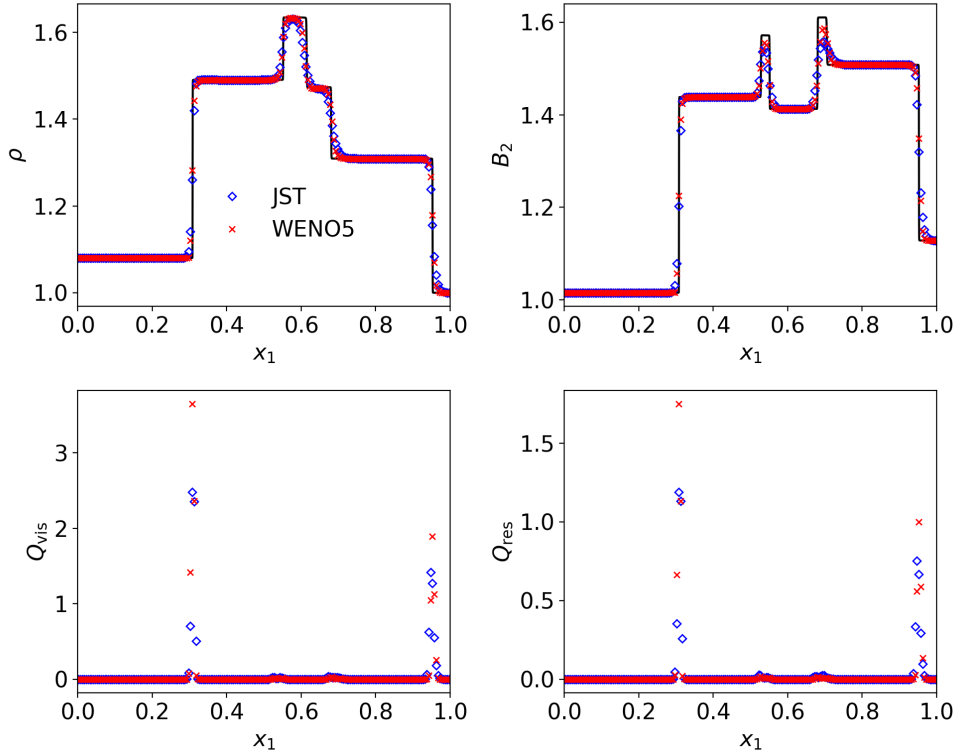


Figure 5: One-dimensional Dai–Woodward’s shock tube problem using 200 grid points. Shown are the mass density (top left panel), the y-component of magnetic field (top right panel), the viscous heating rate (bottom left panel), and the resistive heating rate (bottom right panel) at $t = 0.2$ for the JST-Roe scheme (blue diamond) and the WENO5-Roe scheme (red cross). The solid lines indicate the reference solution calculated with the WENO5 scheme using 4000 grid points.

the compound shock and slow shock at $x \sim 0.65$. Note that the ratio between the viscous and resistive heating rates depends on the dissipation methods (e.g., LLF or Roe).

4.4. Two-dimensional MHD Orszag–Tang vortex problem

Multi-dimensional MHD problems suffer from the numerical error in the divergence of the magnetic field. The robustness and energy-conservation of the proposed schemes in the two-dimensional domain are tested using the Orszag–Tang vortex problem [50]. There are minor variations of the numerical settings in the previous literatures. The numerical setup used in this paper is identical to that of Ryu et al. [51, 52]. The numerical solution is shown in Fig. 7. The spatial profiles of gas and magnetic pressures agreed well with the previous reports (e.g., Fig. 3 of Ryu et al. [52]). The viscous and resistive heating rates were concentrated near the shock fronts.

When the total energy equation is not directly solved in the MHD schemes, the total energy conservation may be numerically violated. The proposed scheme is designed to satisfy the total energy conservation in terms of the spatial discretization. However, the total energy conservation may be violated by the numerical error of the temporal discretization

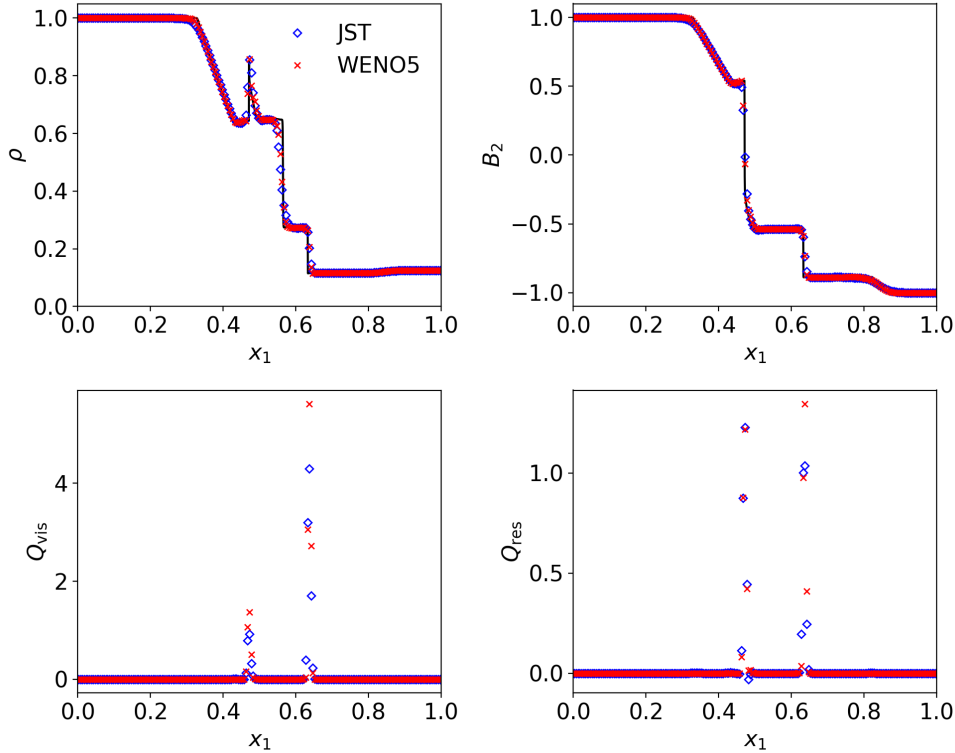


Figure 6: One-dimensional Brio–Wu’s shock tube problem using 200 grid points. Shown are the mass density (top left panel), the y-component of magnetic field (top right panel), the viscous heating rate (bottom left panel), and the resistive heating rate (bottom right panel) at $t = 0.1$ for the JST-Roe scheme (blue diamond) and the WENO5-Roe scheme (red cross). The solid lines indicate the reference solution calculated with the WENO5 scheme using 4000 grid points.

as discussed in Sec. 3.1. In our formulation, the conservation error of the total energy depends only on the discretization error of the time integration scheme. Because the third-order Runge-Kutta method was used for time integration, the conservation error of the total energy should converge by third order against the size of time step used in the simulations. The convergence of the total energy conservation in terms of the Courant number of the time step criterion is shown in Fig. 8. Here, we employed the lower spatial resolution with 128×128 grid points to reduce the computational cost. The observed third-order convergence of the conservation error of the total energy is consistent with our expectation.

We also checked the conservation error of the momentum. Due to the spatial symmetry of this test problem, the conservation error of the momentum was kept constant in the round-off error. Instead, we evaluated the physical part of the Lorentz force Eq. 9 and the artificial field-aligned force $B_i \nabla \cdot \mathbf{B}$. The standard deviation (in time and space) of the x -component of the field-aligned force was several tens of percent of the physical part of the Lorentz force. The amount of this field-aligned force is a direct consequence of the numerical $\nabla \cdot \mathbf{B}$ error, which depends on the filtering scheme, the spatial resolution, and the parameters of the divergence cleaning method (c_ψ and τ_ψ in this study). As we discussed in Sec. 2.7,

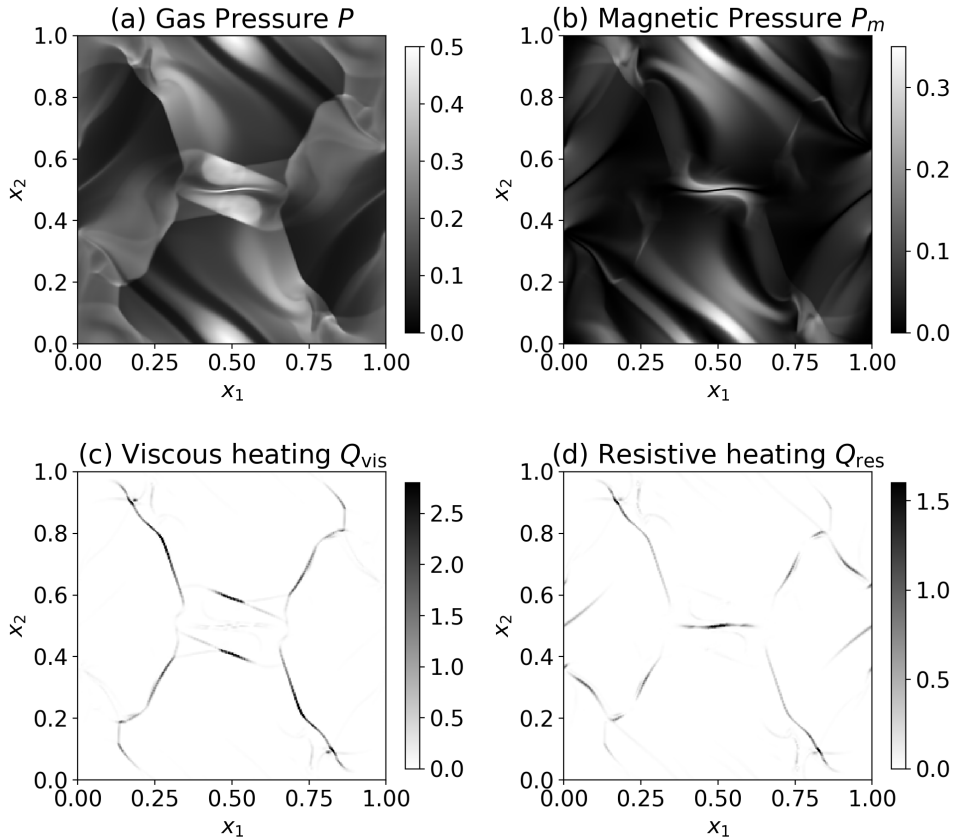


Figure 7: Two-dimensional Orszag–Tang vortex problem calculated with the WENO5-Roe scheme using 256×256 grid points. Shown are (a) the gas pressure, (b) the magnetic pressure, (c) the viscous heating rate, and (d) the resistive heating rate at $t = 0.48$.

the present scheme can be modified so that the momentum conservation is satisfied even when $\nabla \cdot \mathbf{B}$ is nonzero. This alternative version may be used in the problems where the strict momentum conservation by the Lorentz force is required.

One of the advantages of the proposed scheme is that the analysis of the energy variations in the numerical solution can be accurate and straightforward. Figure 9 shows the temporal variation of the internal, kinetic, and magnetic energies and the contributions to their variation. The initial kinetic energy is converted into the internal and magnetic energies during the time evolution. The prominent energy exchange is through the works by the pressure gradient and Lorentz forces. Both the pressure gradient force the viscous heating convert the kinetic energy into the internal energy. The temporal change of the magnetic energy is dominated by the work done by the Lorentz force. The resistive heating has only minor effect in the energy conversion. The heating from the $\nabla \cdot \mathbf{B}$ error, i.e., Q_ψ , is negligible (less than 4×10^{-4} as the volume-averaged value). This small contribution of Q_ψ can be explained that this value is roughly proportional to the square of the divergence of the magnetic field. For each energy equation, all the contributions are fully balanced, indicating the accuracy

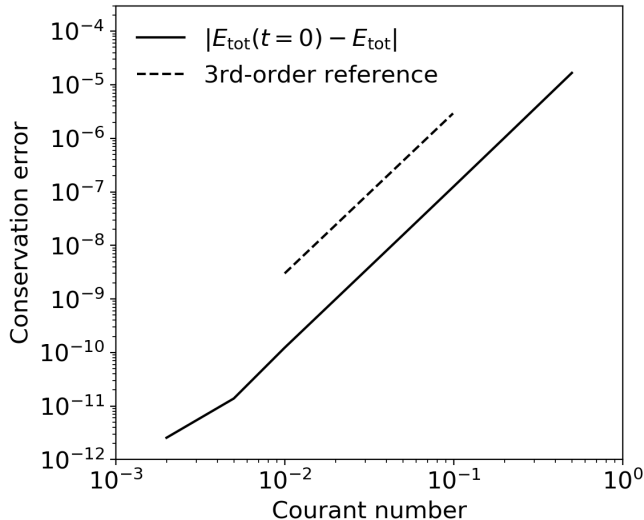


Figure 8: Conservation error of the total energy for Orszag–Tang vortex problem calculated with the WENO5-Roe scheme using 128×128 grid points. Shown is difference between the initial ($t = 0$) and final step ($t = 0.48$) of the volume-averaged total energy density.

of the energy analysis presented here.

4.5. Two-dimensional MHD blast problem

The two-dimensional MHD blast wave problem proposed by Balsara & Spicer [53] is one of the most stringent among the standard test problems. In the original version, the plasma beta (i.e., the ratio between the gas pressure and magnetic pressure) in the ambient is set to approximately 2.5×10^{-4} . This problem is a severe numerical benchmark for the MHD solvers because the positivity of the gas pressure can be easily violated due to the shock propagation in the extremely strong magnetic field. We found that the JST-Roe, JST-LLF, and WENO5-LLF schemes can handle this problem successfully, whereas the WENO5-Roe scheme failed due to the negative pressure during the time integration.

To assess the further robustness of the proposed schemes, we calculated the MHD blast problem in the non-standard setting with a lower plasma beta. The initially uniform mass density, velocity, and magnetic field are imposed as $(\rho, V_1, V_2, B_1, B_2) = (1, 0, 0, 100/\sqrt{4\pi}, 0)$. The initial gas pressure is set to 10^{-5} except in a central circle of radius 0.1, where the pressure is set to 1000. The only difference from the original problem [53] is the much lower gas pressure in the ambient region. The resultant plasma beta in the ambient region is 2.5×10^{-8} , which is the most stringent setup among the family of the MHD blast wave problems tested in previous literatures [53, 35, 54, 55]. The numerical solution obtained by 256×256 grid points with JST-Roe scheme is shown in Fig. 10. The JST-Roe and JST-LLF schemes can handle this problem, but WENO5-LLF scheme causes a negative pressure during the time integration. We found that the two JST schemes are extremely robust in this problem and stable even when we set the ambient gas pressure to 10^{-7} (i.e., the ambient

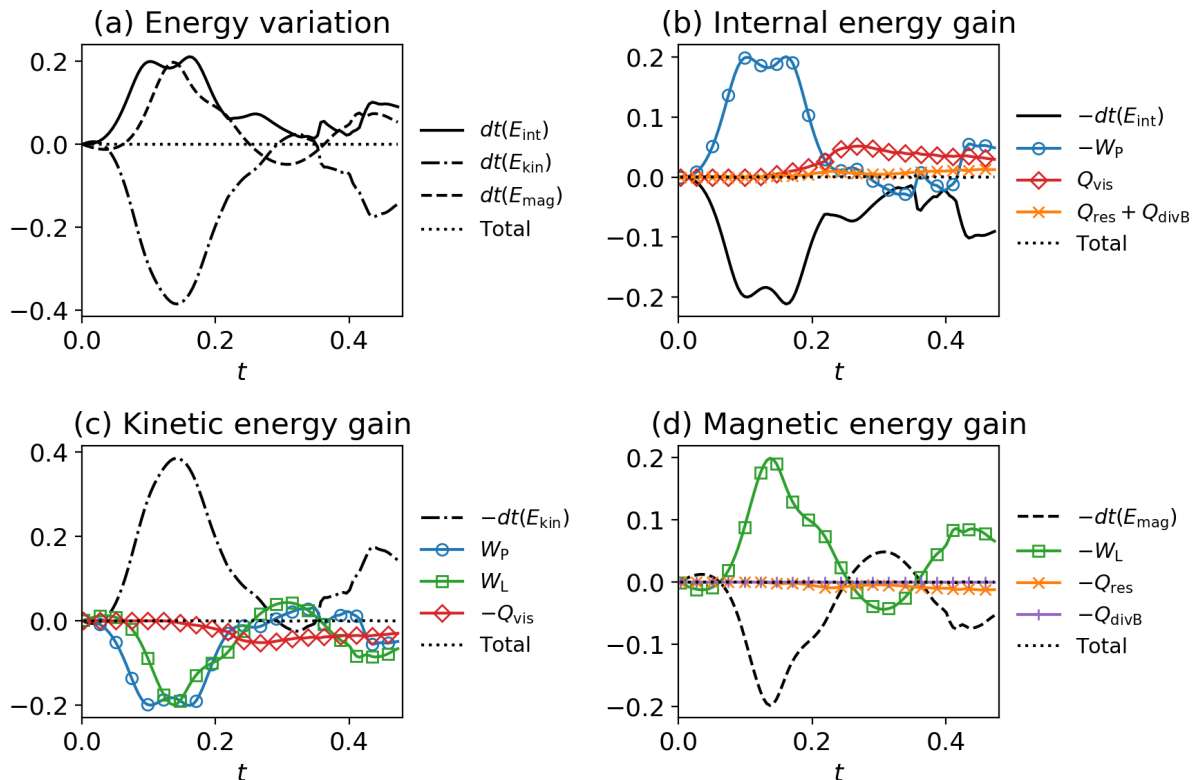


Figure 9: Contributions in energy equations for Orszag–Tang vortex problem calculated with the WENO5-Roe scheme using 256×256 grid points. Shown are (a) the temporal variation of volume-averaged energy densities, (b) the gain and loss of internal energy, (c) the gain and loss of kinetic energy, and (d) the gain and loss of magnetic energy.

plasma beta of 2.5×10^{-10}).

4.6. Two-dimensional MHD Rotor problem

The two-dimensional MHD rotor problem originally proposed by Balsara & Spicer [53] involves a rotating disk with an initial magnetic field perpendicular to the rotation axis. The strong rotational discontinuities along with the shocks and rarefactions are generated by the shearing and expansion motion of the rotating disk. Among the several variations of this problem, the second rotor test described by Tóth [23] was selected for this study. All of the proposed schemes (JST-Roe, JST-LLF, WENO5-Roe, and WENO5-LLF) are capable of solving this problem.

A non-standard alternative of the rotor problem with more stringent parameter was also carried out. The numerical setup is identical to that of the Tóth’s second rotor problem [23] except the initial gas pressure and linear taper. The initial gas pressure is uniformly set to 5×10^{-4} whereas it is 0.5 in the original problem. The initial plasma beta is about 2.0×10^{-3} . The linear taper is applied between a radius of 0.1 and a radius of 0.13 so that the rotor’s velocity and mass density linearly approach to the background over six grid points when the

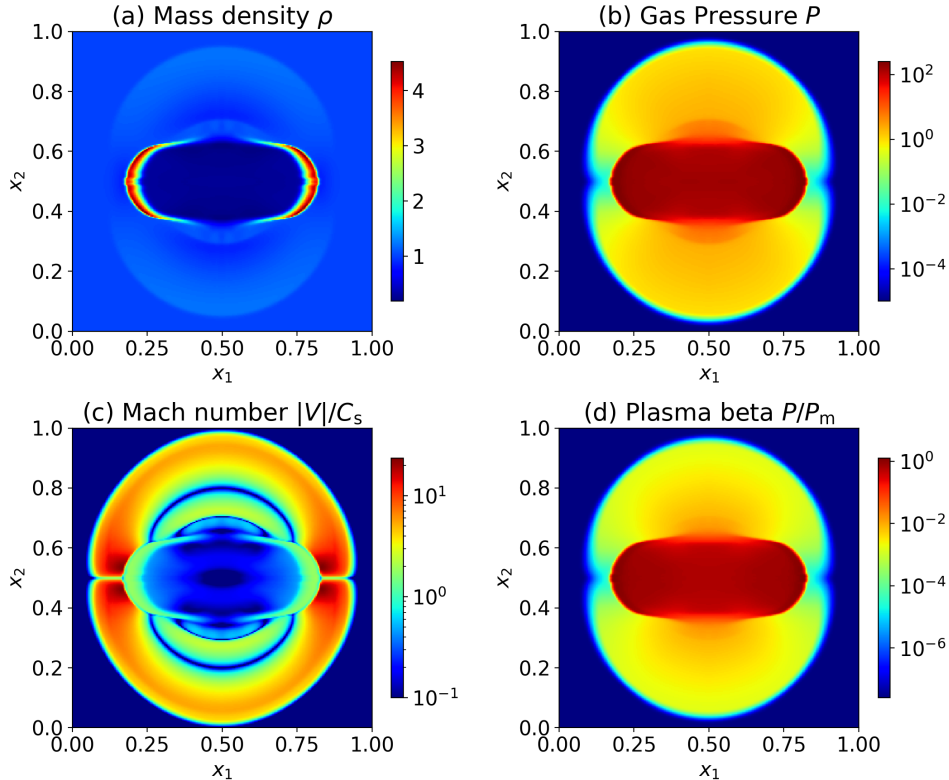


Figure 10: Two-dimensional MHD blast problem calculated with the JST-Roe scheme using 256×256 grid points. Shown are (a) the mass density, (b) the gas pressure, (c) the Mach number, and (d) the plasma beta at $t = 0.01$. The range of the color map is determined by the maximum and minimum values at the snapshot (except the lower range of 0.1 in panel c).

problem is solved with 200×200 grid points. Figure 11 shows the numerical solution solved by the WENO5-LLF scheme. The expansion of the rotating disk caused the region with very low pressure near the center of the numerical domain. At the final snapshot ($t = 0.295$), the plasma beta was lower than 2×10^{-4} and the local Mach number exceeds 150 in the low-pressure region. These values of the Mach number and plasma beta are more severe than those used in previous studies [53, 35, 54, 55], making the problem a severe benchmark for the numerical robustness.

We found that two JST schemes and the WENO5-Roe scheme failed to handle this problem with the initial gas pressure of 5×10^{-4} . By changing the initial gas pressure from 0.5 to 5×10^{-4} multiplying a factor of 0.1 in each step, we checked the minimum gas pressure that the numerical scheme can handle this problem. The minimum values of the initial gas pressure that can be handled by the JST-LLF, JST-Roe, and WENO5-Roe schemes were 10^{-3} , 10^{-2} , and 10^{-1} , respectively. The poor robustness of the JST-Roe and WENO5-Roe schemes can be explained that the viscous and resistive heating can be negative for the Roe-type model. The higher robustness of the WENO5-LLF scheme over the JST-LLF scheme may have been caused by the higher gradient of the solution (see panel a in Fig. 11). We

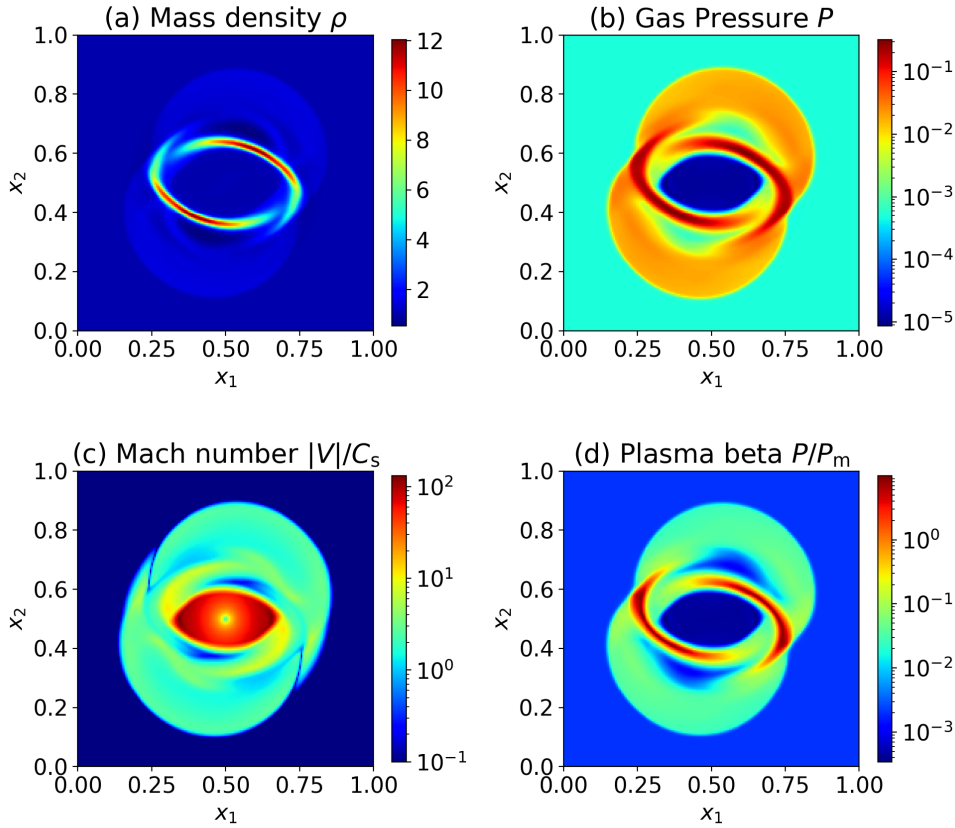


Figure 11: Two-dimensional MHD rotor problem calculated with the WENO5-LLF scheme using 200×200 grid points. Shown are (a) the mass density, (b) the gas pressure, (c) the Mach number, and (d) the plasma beta at $t = 0.295$. The range of the color map is determined by the maximum and minimum values at the snapshot (except the lower range of 0.1 in panel c).

found that the JST-LLF and JST-Roe schemes can solve the problem with the initial gas pressure of 5×10^{-4} and 5×10^{-3} , respectively, when the finer numerical mesh of 400×400 grid points is used. We found no improvement of the numerical robustness for the two WENO5 schemes with 400×400 grid points.

5. Conclusions

We have presented an energy-consistent formulation of the compressible magnetohydrodynamic equations. The transport and interaction of the internal, kinetic, and magnetic energies are satisfied in the discrete sense, while maintaining the standard conservation property of the mass, momentum, magnetic flux, and total energy. These characteristics have been accomplished through the application of a simple constructive strategy of using the discrete versions of the product rule. The shock capturing was achieved by introducing the nonlinear filtering flux in the discretized equations. The energy-consistent formulation of

the nonlinear filtering flux for both hydrodynamic and MHD equations was also suggested. The viscous and resistive heating rates become positive when the filtering flux satisfies the specific conditions.

The proposed formulations were implemented with the spatially second-order and the sixth-order central difference operators. The filtering flux is developed based the second-order JST scheme and fifth-order WENO reconstruction with the LLF-type and Roe-type filtering schemes. All of these schemes are integrated by the third-order SSP Runge-Kutta method. The combination of the energy-consistent finite difference formulation and the appropriate filtering with small numerical overshoot was shown to yield the excellent robustness for the most stringent problems.

In this study, we assume the periodic boundary conditions in all test problems presented in Sec. 4. The conservation property of the (magneto)hydrodynamic variables is affected by the non-periodic boundary conditions in practical problems. For the practical implementation of the non-periodic boundary conditions in the finite difference schemes with the secondary conservation property, we refer the reader to the discussion in Morinishi [2] and Desjardins [14].

Acknowledgements

This work was supported by JSPS KAKENHI grant No. JP19K14756. A major part of numerical computations was carried out on Cray XC50 at Center for Computational Astrophysics, National Astronomical Observatory of Japan. This work was supported by the computational joint research program of the Institute for Space-Earth Environmental Research (ISEE), Nagoya University. Some numerical computations were carried out on the FX100/Flow supercomputer system at the Information Technology Center, Nagoya University. Analysis of the numerical simulations were carried out in the Center for Integrated Data Science, Institute for Space-Earth Environmental Research, Nagoya University through the joint research program.

References

- [1] F. H. Harlow, J. E. Welch, Numerical Calculation of Time-Dependent Viscous Incompressible Flow of Fluid with Free Surface, *Physics of Fluids* 8 (12) (1965) 2182–2189. doi:10.1063/1.1761178.
- [2] Y. Morinishi, T. S. Lund, O. V. Vasilyev, P. Moin, Fully Conservative Higher Order Finite Difference Schemes for Incompressible Flow, *Journal of Computational Physics* 143 (1) (1998) 90–124. doi:10.1006/jcph.1998.5962.
- [3] Y. Morinishi, O. V. Vasilyev, T. Ogi, Fully conservative finite difference scheme in cylindrical coordinates for incompressible flow simulations, *Journal of Computational Physics* 197 (2) (2004) 686–710. doi:10.1016/j.jcp.2003.12.015.
- [4] A. G. Kravchenko, P. Moin, On the Effect of Numerical Errors in Large Eddy Simulations of Turbulent Flows, *Journal of Computational Physics* 131 (2) (1997) 310–322. doi:10.1006/jcph.1996.5597.
- [5] C. A. Kennedy, A. Gruber, Reduced aliasing formulations of the convective terms within the Navier-Stokes equations for a compressible fluid, *Journal of Computational Physics* 227 (3) (2008) 1676–1700. doi:10.1016/j.jcp.2007.09.020.
- [6] S. Pirozzoli, Numerical Methods for High-Speed Flows, *Annual Review of Fluid Mechanics* 43 (1) (2011) 163–194. doi:10.1146/annurev-fluid-122109-160718.

- [7] A. Jameson, W. Schmidt, E. Turkel, Numerical solution of the Euler equations by finite volume methods using Runge Kutta time stepping schemes (Jun. 1981).
- [8] F. Ducros, F. Laporte, T. Soulères, V. Guinot, P. Moinat, B. Caruelle, High-Order Fluxes for Conservative Skew-Symmetric-like Schemes in Structured Meshes: Application to Compressible Flows, *Journal of Computational Physics* 161 (1) (2000) 114–139. doi:10.1006/jcph.2000.6492.
- [9] A. Jameson, The construction of discretely conservative finite volume schemes that also globally conserve energy or entropy, *Journal of Scientific Computing* 34 (2) (2008) 152–187.
- [10] A. Jameson, Formulation of kinetic energy preserving conservative schemes for gas dynamics and direct numerical simulation of one-dimensional viscous compressible flow in a shock tube using entropy and kinetic energy preserving schemes, *Journal of Scientific Computing* 34 (2) (2008) 188–208.
- [11] S. Pirozzoli, Generalized conservative approximations of split convective derivative operators, *Journal of Computational Physics* 229 (19) (2010) 7180–7190. doi:10.1016/j.jcp.2010.06.006.
- [12] J. C. Kok, A high-order low-dispersion symmetry-preserving finite-volume method for compressible flow on curvilinear grids, *Journal of Computational Physics* 228 (18) (2009) 6811–6832. doi:10.1016/j.jcp.2009.06.015.
- [13] Y. Morinishi, Skew-symmetric form of convective terms and fully conservative finite difference schemes for variable density low-Mach number flows, *Journal of Computational Physics* 229 (2) (2010) 276–300. doi:10.1016/j.jcp.2009.09.021.
- [14] O. Desjardins, G. Blanquart, G. Balarac, H. Pitsch, High order conservative finite difference scheme for variable density low Mach number turbulent flows, *Journal of Computational Physics* 227 (15) (2008) 7125–7159. doi:10.1016/j.jcp.2008.03.027.
- [15] Y. Kuya, K. Totani, S. Kawai, Kinetic energy and entropy preserving schemes for compressible flows by split convective forms, *Journal of Computational Physics* 375 (2018) 823–853. doi:10.1016/j.jcp.2018.08.058.
- [16] H. C. Yee, N. D. Sandham, M. J. Djomehri, Low-Dissipative High-Order Shock-Capturing Methods Using Characteristic-Based Filters, *Journal of Computational Physics* 150 (1) (1999) 199–238. doi:10.1006/jcph.1998.6177.
- [17] T. Shiroto, S. Kawai, N. Ohnishi, Structure-preserving operators for thermal-nonequilibrium hydrodynamics, *Journal of Computational Physics* 364 (2018) 1–17. arXiv:1705.03136, doi:10.1016/j.jcp.2018.03.008.
- [18] M.-J. Ni, R. Munipalli, N. B. Morley, P. Huang, M. A. Abdou, A current density conservative scheme for incompressible MHD flows at a low magnetic Reynolds number. Part I: On a rectangular collocated grid system, *Journal of Computational Physics* 227 (1) (2007) 174–204. doi:10.1016/j.jcp.2007.07.025.
- [19] M.-J. Ni, R. Munipalli, P. Huang, N. B. Morley, M. A. Abdou, A current density conservative scheme for incompressible MHD flows at a low magnetic Reynolds number. Part II: On an arbitrary collocated mesh, *Journal of Computational Physics* 227 (1) (2007) 205–228. doi:10.1016/j.jcp.2007.07.023.
- [20] M.-J. Ni, J.-F. Li, A consistent and conservative scheme for incompressible MHD flows at a low magnetic Reynolds number. Part III: On a staggered mesh, *Journal of Computational Physics* 231 (2) (2012) 281–298. doi:10.1016/j.jcp.2011.08.013.
- [21] Y. Idomura, M. Ida, S. Tokuda, L. Villard, New conservative gyrokinetic full- f Vlasov code and its comparison to gyrokinetic δf particle-in-cell code, *Journal of Computational Physics* 226 (1) (2007) 244–262. doi:10.1016/j.jcp.2007.04.013.
- [22] T. Shiroto, N. Ohnishi, Y. Sentoku, Quadratic conservative scheme for relativistic Vlasov-Maxwell system, *Journal of Computational Physics* 379 (2019) 32–50. arXiv:1802.07238, doi:10.1016/j.jcp.2018.10.041.
- [23] G. Tóth, The $\nabla \cdot \mathbf{B} = 0$ Constraint in Shock-Capturing Magnetohydrodynamics Codes, *Journal of Computational Physics* 161 (2000) 605–652. doi:10.1006/jcph.2000.6519.
- [24] A. Dedner, F. Kemm, D. Kröner, C.-D. Munz, T. Schnitzer, M. Wesenberg, Hyperbolic Divergence Cleaning for the MHD Equations, *Journal of Computational Physics* 175 (2002) 645–673. doi:10.1006/jcph.2001.6961.
- [25] A. Jameson, Origins and further development of the jameson–schmidt–turkel scheme, *AIAA Journal*

- (2017) 1487–1510.
- [26] R. C. Swanson, E. Turkel, On central-difference and upwind schemes, in: *Upwind and High-Resolution Schemes*, Springer, 1992, pp. 167–181.
 - [27] A. Jameson, Analysis and Design of Numerical Schemes for Gas Dynamics, 1: Artificial Diffusion, Upwind Biasing, Limiters and Their Effect on Accuracy and Multigrid Convergence, *International Journal of Computational Fluid Dynamics* 4 (3) (1995) 171–218. doi:10.1080/10618569508904524.
 - [28] B. van Leer, Towards the Ultimate Conservation Difference Scheme. II. Monotonicity and Conservation Combined in a Second-Order Scheme, *Journal of Computational Physics* 14 (4) (1974) 361–370. doi:10.1016/0021-9991(74)90019-9.
 - [29] G.-S. Jiang, C.-W. Shu, Efficient Implementation of Weighted ENO Schemes, *Journal of Computational Physics* 126 (1996) 202–228. doi:10.1006/jcph.1996.0130.
 - [30] C.-W. Shu, S. Osher, Efficient Implementation of Essentially Non-oscillatory Shock-Capturing Schemes, *Journal of Computational Physics* 77 (2) (1988) 439–471. doi:10.1016/0021-9991(88)90177-5.
 - [31] S. Gottlieb, D. I. Ketcheson, C.-W. Shu, High order strong stability preserving time discretizations, *Journal of Scientific Computing* 38 (3) (2009) 251–289. doi:10.1007/s10915-008-9239-z.
 - [32] A. Jameson, T. Baker, Solution of the euler equations for complex configurations, in: *6th Computational Fluid Dynamics Conference Danvers*, 1983, p. 1929.
 - [33] A. Suresh, H. T. Huynh, Accurate Monotonicity-Preserving Schemes with Runge Kutta Time Stepping, *Journal of Computational Physics* 136 (1997) 83–99. doi:10.1006/jcph.1997.5745.
 - [34] D. S. Balsara, Linearized Formulation of the Riemann Problem for Adiabatic and Isothermal Magnetohydrodynamics, *The Astrophysical Journal Supplement Series* 116 (1) (1998) 119–131. doi:10.1086/313092.
 - [35] J. M. Stone, T. A. Gardiner, P. Teuben, J. F. Hawley, J. B. Simon, Athena: A New Code for Astrophysical MHD, *The Astrophysical Journal Supplement Series* 178 (1) (2008) 137–177. arXiv:0804.0402, doi:10.1086/588755.
 - [36] P. D. Lax, Weak solutions of nonlinear hyperbolic equations and their numerical computation, *Communications on pure and applied mathematics* 7 (1) (1954) 159–193.
 - [37] A. Kurganov, E. Tadmor, New High-Resolution Central Schemes for Nonlinear Conservation Laws and Convection-Diffusion Equations, *Journal of Computational Physics* 160 (1) (2000) 241–282. doi:10.1006/jcph.2000.6459.
 - [38] P. L. Roe, Approximate riemann solvers, parameter vectors, and difference schemes, *Journal of computational physics* 43 (2) (1981) 357–372.
 - [39] D. Ryu, T. W. Jones, Numerical magnetohydrodynamics in astrophysics: Algorithm and tests for one-dimensional flow', *The Astrophysical Journal* 442 (1995) 228–258. arXiv:astro-ph/9404074, doi:10.1086/175437.
 - [40] A. Harten, J. M. Hyman, Self-Adjusting Grid Methods for One-Dimensional Hyperbolic Conservation Laws, *Journal of Computational Physics* 50 (2) (1983) 235–269. doi:10.1016/0021-9991(83)90066-9.
 - [41] A. Harten, B. Engquist, S. Osher, S. R. Chakravarthy, Uniformly High Order Accurate Essentially Non-oscillatory Schemes, III, *Journal of Computational Physics* 131 (1) (1997) 3–47. doi:10.1006/jcph.1996.5632.
 - [42] A. Mignone, P. Tzeferacos, G. Bodo, High-order conservative finite difference GLM-MHD schemes for cell-centered MHD, *Journal of Computational Physics* 229 (17) (2010) 5896–5920. arXiv:1001.2832, doi:10.1016/j.jcp.2010.04.013.
 - [43] C.-W. Shu, S. Osher, Efficient Implementation of Essentially Non-oscillatory Shock-Capturing Schemes, II, *Journal of Computational Physics* 83 (1) (1989) 32–78. doi:10.1016/0021-9991(89)90222-2.
 - [44] D. S. Balsara, Second-Order-accurate Schemes for Magnetohydrodynamics with Divergence-free Reconstruction, *The Astrophysical Journal Supplement Series* 151 (2004) 149–184. arXiv:astro-ph/0308249, doi:10.1086/381377.
 - [45] M. Dumbser, D. S. Balsara, E. F. Toro, C.-D. Munz, A unified framework for the construction of one-step finite volume and discontinuous Galerkin schemes on unstructured meshes, *Journal of Computational Physics* 227 (2008) 8209–8253. doi:10.1016/j.jcp.2008.05.025.

- [46] R. Borges, M. Carmona, B. Costa, W. S. Don, An improved weighted essentially non-oscillatory scheme for hyperbolic conservation laws, *Journal of Computational Physics* 227 (2008) 3191–3211. doi:10.1016/j.jcp.2007.11.038.
- [47] G. A. Sod, Review. A Survey of Several Finite Difference Methods for Systems of Non-linear Hyperbolic Conservation Laws, *Journal of Computational Physics* 27 (1) (1978) 1–31. doi:10.1016/0021-9991(78)90023-2.
- [48] W. Dai, P. R. Woodward, On the Divergence-free Condition and Conservation Laws in Numerical Simulations for Supersonic Magnetohydrodynamical Flows, *The Astrophysical Journal* 494 (1998) 317–335. doi:10.1086/305176.
- [49] M. Brio, C. C. Wu, An upwind differencing scheme for the equations of ideal magnetohydrodynamics, *Journal of Computational Physics* 75 (1988) 400–422. doi:10.1016/0021-9991(88)90120-9.
- [50] S. A. Orszag, C. M. Tang, Small-scale structure of two-dimensional magnetohydrodynamic turbulence, *Journal of Fluid Mechanics* 90 (1979) 129–143. doi:10.1017/S002211207900210X.
- [51] D. Ryu, T. W. Jones, A. Frank, Numerical Magnetohydrodynamics in Astrophysics: Algorithm and Tests for Multidimensional Flow, *The Astrophysical Journal* 452 (1995) 785. arXiv:astro-ph/9505073, doi:10.1086/176347.
- [52] D. Ryu, F. Miniati, T. W. Jones, A. Frank, A Divergence-free Upwind Code for Multidimensional Magnetohydrodynamic Flows, *The Astrophysical Journal* 509 (1998) 244–255. arXiv:astro-ph/9807228, doi:10.1086/306481.
- [53] D. S. Balsara, D. S. Spicer, A Staggered Mesh Algorithm Using High Order Godunov Fluxes to Ensure Solenoidal Magnetic Fields in Magnetohydrodynamic Simulations, *Journal of Computational Physics* 149 (1999) 270–292. doi:10.1006/jcph.1998.6153.
- [54] D. S. Balsara, Divergence-free reconstruction of magnetic fields and WENO schemes for magnetohydrodynamics, *Journal of Computational Physics* 228 (2009) 5040–5056. arXiv:0811.2192, doi:10.1016/j.jcp.2009.03.038.
- [55] D. Lee, A solution accurate, efficient and stable unsplit staggered mesh scheme for three dimensional magnetohydrodynamics, *Journal of Computational Physics* 243 (2013) 269–292. arXiv:1303.6988, doi:10.1016/j.jcp.2013.02.049.